nature immunology

Supplementary information

https://doi.org/10.1038/s41590-024-02059-6

Integrating single-cell RNA and T cell/B cell receptor sequencing with mass cytometry reveals dynamic trajectories of human peripheral immune cells from birth to old age

In the format provided by the authors and unedited

Supplementary Information

1. Supplementary Results

1.1. The role of *S100A4* in an *in vitro* aging model

We investigated the role of M-DEG *S100A4* in a long-term passage-induced *in vitro* aging model[1]. As expected, the senescence-associated (SA)-β-Galactosidase (SA-β-Gal) activities and senescence-associated secretory phenotype (SASP)-related genes (*IL1A*, *IL6*, *CXCL8*, and *CCL2*) expression levels were significantly upregulated in late passage (i.e., passage 7 and passage 9) human umbilical vascular endothelial cells (HUVECs) (Supplementary Fig. 1a, b). Specifically, the mRNA levels of *S100A4* were markedly increased in a time-course dependent manner (Supplementary Fig. 1c). Further, targeting *S100A4* by siRNA in HUVECs significantly reduced late passage-induced upregulation of SA-β-Gal activities and SASP-related genes expression levels (Supplementary Fig. 1d–f), suggesting that *S100A4* acted as a positive regulator in the aging process.

1.2. Rewiring of cell–cell interactions (CCIs) among peripheral immune cells across the lifespan

Immunological processes involve interactions between various immune cell types to coordinate the behavior of immune cells during an immune response[2, 3]. To characterize the dynamics of CCIs among immune cells across the lifespan, we calculated the CCI probabilities (reflecting the communication probability between two cells[4, 5]) among all pairs of cell subsets based on the expression of known ligands and receptors in each sample (Supplementary Methods). Human ligand–receptor interaction pairs were downloaded from the CellTalkDB database[6]. The CCIs that significantly varied among the eight human life stages (Kruskal–Wallis test, FDR-adjusted $P < 0.0001$) were determined by comparing the CCI probabilities of all cell subset pairs in each sample (Fig. 3a). Among cell subset pairs whose CCI probability significantly changed with ages, we found that T cells experienced the most intensive rewiring in cell–cell interactions with age (Fig. 3b). Using hierarchical clustering, the significantly varied CCIs were clustered into four clusters, each of which was enriched in specific life stages. The interaction hubs of each cluster were different (Fig. 3a–f). The results showed that: 1) The CCI probabilities of cluster 1 peaked in the UCB group, and the interaction hub of this cluster was NK_CD56^{high} (Fig. 3a, c). NK_CD56^{high} cells were known to be cytokine-producer and serve as immunoregulators[7]. 2) The CCI probabilities of cluster 2 peaked in children (1–8y), and the interaction hub of this cluster became

CD8_TEM_ZNF683 (Fig. 3a, d). ZNF683 is upregulated in T cells with cytotoxic characteristics, and higher expression of ZNF683 promotes $CD8^+$ T cell IFN-γ secretion and proliferation after infection[8]. 3) The CCI probabilities of cluster 3 were significantly upregulated in adolescents and adults (12–60 y), and the interaction hub of this cluster was CD4_TEM_ANXA1 cells (Fig. 3a, e). $CD4^+$ T cells expressing ANXA1 have been reported to attenuate T cell-driven inflammatory responses via intracellular signaling[9]. 4) The CCI probabilities of cluster 4 were significantly upregulated in elderly (70–over 90 y), and the interaction hub changed to CD4_TEM_GNLY cells (Fig. 3a, f). Cytotoxic $CD4^+$ T cells were found to have the ability of eliminating senescent cells[10]. Thus, the CCIs among various peripheral immune cell subsets displayed different patterns at different stages across the lifespan, suggestive of the different task priorities immune system has to set at different life stages.

Furthermore, over 800 differentially expressed ligands and receptors among the eight life stages (Kruskal–Wallis test, $P < 0.05$) were identified (Supplementary Table 8). Subsequently, an age-modulated CCI network was constructed, which was mediated by differentially expressed ligand–receptor pairs between different peripheral immune cell subsets (Fig. 3g). A total of 31 known immune checkpoint targets in cancer immunotherapy[33] were identified among these differentially expressed ligands and receptors. Functional enrichment analyses showed that these differentially expressed ligands and receptors were enriched in biological processes related to the regulation of lymphocyte activation, T cell activation, leukocyte cell–cell adhesion, and leukocyte proliferation pathways (Fig. 3h). Next, the topological characteristics of the CCI network were examined using Cytoscape[11], which enables visualization and analyses of the importance of genes within interaction networks. The immune checkpoints had higher node degree[12] and lower average shortest path length[13] than non-immune checkpoints (Fig. 3i). The higher node degrees and lower average shortest path length of immune checkpoints indicated that they hold higher possibility to be hubs involved in more competing interactions in CCIs, and may act as bridges connecting different network components and facilitating cellular communication[12, 13]. Moreover, the expression of these immune checkpoints was markedly altered across the lifespan in multiple cell subsets, particularly in T-cell subsets (Fig. 3j–l, Extended Data Fig. 5, and Supplementary Table 9). For example, the expression of the co-stimulatory checkpoint *CD27* and *ICOS* and co-inhibitory checkpoint *PDCD1* (Fig. 3k), three promising immune-modulatory targets in cancer treatment[14], showed a decreased trend with age in multiple T-cell subsets. To validate these age-

related immune checkpoint receptors at the single-cell protein level, we performed CyTOF profiling in different age groups. As shown in Fig. 3l, the protein expression dynamics detected by CyTOF profiling (i.e., CD27, ICOS, and PD-1) were in agreement with the gene expression dynamics detected by scRNA-seq (i.e., *CD27*, *ICOS*, and *PDCD1*). Our results indicate that immune checkpoints play a more critical role in the age-modulated CCI network compared with non-immune checkpoints. Furthermore, alterations of immune checkpoints across the whole human lifespan mainly occur in T cells and might play essential roles during human development and aging.

1.3. Experimental validation of cytotoxic B-cell subset (B_BCR$^+$GNLY$^+$ cells)

Among the BCR-positive cell subsets, we detected a newly identified and unique B-cell subset (B_BCR$^+$GNLY$^+$ cells) that simultaneously expressed B-cell markers and canonical cytotoxic genes (such as *GNLY*). Granulysin is a saposin-like pore-forming protein with antimicrobial and antitumor cytotoxic activity; its expression is restricted to cytotoxic immune cells such as cytotoxic CD8$^+$ T cells, NK cells, and γδ T cells[15]. The role of granulysin in B-cell-mediated functions has yet to be reported. We therefore sought to determine whether B_BCR$^+$GNLY$^+$ cells possess cytotoxic functions. Because these cells express cytotoxic proteins (i.e., marker protein granulysin) that are localized in the cytoplasm, cell membrane perforation during purification may negatively affect viability. Given this technical difficulty to obtain fresh cells for cytotoxic experiments, we overexpressed the granulysin-encoding gene *GNLY* in human B cells and tested their killing effects on *Staphylococcus Aureus* (*S. aureus*) and *Streptococcus Pneumoniae* (*S. pneumoniae*) (Supplementary Fig. 3a). Although no differences were observed in bacterial survival between the controls, GNLY-overexpressing B cells significantly reduced bacterial colonies compared with control-transfected B cells and non-transfected B cells (Supplementary Fig. 3b). Moreover, B cells isolated from transgenic mice overexpressing human *GNLY* exhibited cytotoxic effects on *S. aureus* and *S. pneumoniae* (Supplementary Fig. 3c–e).

Next, to investigate the functional differences between the newly identified cytotoxic B-cell subset (B_BCR$^+$GNLY$^+$ cells) and other immune cells with cytotoxic functions, we compared the gene expression profiles of B_BCR$^+$GNLY$^+$ cells with those of all other cytotoxic peripheral immune cell subsets, including seven cytotoxic T-cell and three cytotoxic NK-cell subsets. The elevation in B-cell signature genes in the B_BCR$^+$GNLY$^+$ cells was expected, while these signature genes

were absent in all other cytotoxic cells from T-cell or NK-cell lineages (Extended Data Fig. 7a, b). Functional enrichment analyses of the DEGs in each cytotoxic cell subset showed that, compared with all other kinds of cytotoxic immune cells, the upregulated DEGs in B_BCR$^+$GNLY$^+$ cells were enriched in the immunoglobulin production, defense response to bacterium, and humoral immune response pathways (Extended Data Fig. 8c, d). It is particularly interesting that B_BCR$^+$GNLY$^+$ cells displayed comparable cytotoxic activities with other cytotoxic cells, actually surpassing several cytotoxic CD8$^+$ T-cell subsets (i.e., CD8_TCM_HAVCR2, CD8_TEM_ZNF683, CD8_TEM_CMC1, and CD8_MAIT_SLC4A10). This was evidenced by the upregulation of the cell killing pathway in B_BCR$^+$GNLY$^+$ cells compared with the abovementioned T- or NK-cell subsets (Extended Data Fig. 7c, d), as well as by gene scoring analyses (Extended Data Fig. 7e). Thus, we have identified a unique B-cell subset (B_BCR$^+$GNLY$^+$ cells) that is enriched in children and expresses cytotoxic genes and BCR genes with potential cytotoxic activities.

Next, we calculated the similarity scores from gene expression profiles among all five B-cell subsets and evaluated the distribution of IgA, IgD, IgG, and IgM in each subset. Among the B-cell subsets, B_BCR$^+$GNLY$^+$ cells were closest to plasma cells, the terminal differentiation step of mature B lymphocytes[16], in terms of both the transcriptome profiles (Supplementary Fig. 3f) and the distribution of immunoglobulin-related genes (Supplementary Fig. 3g). We further explored the potential developmental trajectories of these B-cell subsets by transcriptional similarities using pseudotime trajectory analyses with Monocle2[17]. The B-cell subsets formed a pseudotime trajectory that began with naive B cells, followed by memory B cells and B_BCR$^+$GNLY$^+$ cells, and ended with plasma cells (Supplementary Fig. 3h). There was a continuum of phenotype alterations between memory B cells, B_BCR$^+$GNLY$^+$ cells, and plasma cells. To gain insights into the clonal relationship among the five B-cell subsets, we reconstructed the BCR sequences from scBCR-seq data. The BCR detection rate was high in all five B-cell subsets: 97.13% (B_Naive), 99.61% (Plasma cells), 91.86% (B_Atypical_Memory), 95.54% (B_Memory), and 52.88% (B_BCR$^+$GNLY$^+$); while this rate was absent or extremely low in other PBMC subsets (Extended Data Fig. 8a). We further calculated the average ratio of BCR clones shared between each pair of the B-cell subsets. Plasma cells (16.18%) were the top subset sharing clones with B_BCR$^+$GNLY$^+$ cells, followed by atypical memory B cells (7.29%) (Supplementary Fig. 3i). Four representatively shared BCR clones between these three B-cell subsets are shown in the UAMP plots (Extended

Data Fig. 8b). We further investigated the clone expansion of the B cells during aging used STARTRAC (v0.1.0)[18]. The results showed that B-cell clone expansion primarily occurred during childhood, and mostly concentrated in the newly identified cytotoxic B cells, followed by plasma cells (Extended Data Fig. 8c). No significant differences were observed among the five B-cell subsets in the length distribution of the CDR3 amino acid sequences in BCR heavy- and light-chains (Extended Data Fig. 8d).

To explore the transcriptional regulatory mechanism of cell differentiation in the B-cell subsets, we predicted the core TFs in each subset using SCENIC[19]. Consistent with the gene expression profiles (Supplementary Fig. 3f), the clustering patterns in the TF regulon heatmap revealed that B_BCR$^+$GNLY$^+$ cells were closest to plasma cells in terms of the transcriptional regulatory mechanism (Extended Data Fig. 9a). We determined the top ten TF regulons in each B-cell subset and found that the top ten TFs in B_BCR$^+$GNLY$^+$ and plasma cells were different. The top three TFs in B_BCR$^+$GNLY$^+$ cells were *STAT1*, *IRF1*, and *CEBPB* (Extended Data Fig. 9b). *STAT1* and *IRF1* are associated with cell cytotoxicity[63, 65, 66]. *CEBPB* is involved in the regulatory network of transcription factors that are critical for plasma cell differentiation and survival[20]. However, differing from B_BCR$^+$GNLY$^+$ cells, the top three TFs in plasma cells were *XBP1, CREB3*, and *KLF13* (Extended Data Fig. 9b). *XBP1* and *KLF13* are associated with plasma cell differentiation[21] and B-cell maturation[22], respectively. *CREB3* is a key TF involved in the ER and Golgi stress responses as a regulator of the cell secretory capacity[23] associated with antibody secretion.

Next, we conducted hierarchical clustering on the expression of the top ten TFs in each B-cell subset using heatmaps (Extended Data Fig. 9c). Although the top ten TFs in B_BCR$^+$GNLY$^+$ and plasma cells were different (Extended Data Fig. 9b), the TF expression profiles of the two subsets were closest in the heatmap among all five B-cell subsets (Extended Data Fig. 9c). Taken together, these results indicate that while B_BCR$^+$GNLY$^+$ cells are closest to plasma cells among all the B-cell subsets with respect to gene expression profiles, the distribution of immunoglobulin isotypes, BCR clonotypes, and transcriptional regulatory mechanisms, this newly identified B-cell type has its own distinct characteristics.

1.4. Key genes in single-cell immune age prediction model

The disrupted correlation between the cAge and siAge scores in the diseased indicated the potential ability of our prediction model to present the disrupted immune homeostasis in individuals with

immune-related diseases. To better assess the predictive ability of the siAge model, we defined a fit index that was calculated from the ratio between siAge and cAge. The fit index was used to evaluate the deviations in siAge and cAge between healthy subjects and patients with a disturbed immune function. The median of the fit index in the healthy validation cohorts was close to zero (median fit index, 0.051) (Fig. 7f), indicating that siAge matched cAge in healthy individuals. However, the median fit indices in the NPC, SLE, and KD validation cohorts deviated excessively from zero (Fig. 7f). The median fit index in the NPC cohort (median fit index, −0.113) was significantly lower ($P = 0.022$) than that in the healthy validation cohort (Fig. 7f), indicating that siAge was smaller than cAge and reflected a possible immunosuppressed status in cancer patients[24]. In contrast, the median fit indices in the SLE (median fit index, 1.023) and KD (median fit index, 2.077) validation cohorts were significantly higher than that in the healthy validation cohort ($P = 4.600 \times 10^{-11}$ and $P = 7.300 \times 10^{-5}$, respectively) (Fig. 7f), indicating that siAge was larger than cAge, possibly reflecting a hyperactive immune function in SLE[25] and KD patients[26]. These results indicate that the siAge score can predict the immune status of individuals.

Next, we focused on key genes that were used as inputs to develop the siAge prediction model. These key genes included 21 genes in five cell subsets: *SOX4*, *SVIP*, *PLP2*, *OSTC*, *AHNAK*, *SELENOM*, *SLC25A5*, *LINC00402*, and *GBP5* in CD4_Naive_CCR7 cells; *PLGRKT*, *MLLT11*, *UTP11*, *NPRL3*, *UCP2*, *AAMP*, and *ZCRB1* in CD4_TEM_ZNF683 cells; *SOX4*, *SVIP*, *CD63*, and *PLP2* in CD4_TCM_AQP3 cells; *PLP2*, *NREP*, and *SBDS* in CD8_Naive_ LEF1 cells; and *SELENOK* and *ID2* in CD8_MAIT_SLC4A10 cells (Fig. 7g). These five cell subsets all belonged to T-cell subsets. Of the 21 key genes, ten genes showed an increased expression trend with age; the top three increased genes were protein degradation-related *SVIP*[27] and signal transduction-related *CD63*[28] in CD4_TCM_AQP3 cells, and endoplasmic reticulum-related *PLP2*[29]. The other 11 key genes showed a decreased expression trend with age. The top three decreased genes include cell differentiation-related *SOX4*[30] in CD4_Naive_CCR7 cells and CD4_TCM_AQP3 cells, and two genes *PLGRKT* and *MLLT11* in CD8_TEM_ZNF683 cells. *PLGRKT* is involved in regulation of inflammatory response[31]; while *MLLT11* is involved in regulation of lymphoid development[32]. Furthermore, functional enrichment analyses showed that these 21 key genes were enriched in positive regulation of autophagy, homeostasis of cell number, hormone secretion, and myeloid cell differentiation (Fig. 7i). Recent studies have reported that autophagy is a crucial determinant of cellular health and organismal longevity, and that impairment or imbalance in autophagy promotes

pathological aging and disease[33]. These results suggest that these 21 key genes in T-cell subsets are critical markers for evaluating the immune system over the whole lifespan.

2. Supplementary Discussions

2.1. Biological functions of B_BCR+GNLY+ cells

Traditionally, B cells are thought to be immune cell populations incapable of cytotoxic functions. However, recent studies have reported a "cytotoxic" phenotype of B-cell subsets expressing cytotoxic genes in diseased populations: 1) flow cytometry assays detected a $GZMB^+$ B-cell subset characterized by co-expression of the B-cell marker CD19 and cytotoxic protein granzyme B (with negative expression of granzyme A or granulysin) in peripheral blood of patients with SLE[34] and remitting multiple sclerosis[35] and in lymph nodes of breast cancer patients[36]; and 2) immunofluorescence detected a phenotype of plasma cells ($GZMB^+$ PCs) characterized by co-expression of BCR light chains and cytotoxic protein granzyme B (negative expression of granulysin and low expression of B-cell marker CD19) in human tonsils[37]. However, the $GZMB^+$ B cells and $GZMB^+$ PCs detected by traditional technology in diseased individuals were significantly different from the B_BCR^+GNLY^+ cells discovered through combined scRNA-seq and scBCR-seq analyses in our healthy population. First, the B_BCR^+GNLY^+ cells were characterized by the high expression of BCR genes, *JCHAIN*, and the cytotoxic gene *GNLY* (encoding granulysin). In contrast, granulysin (encoded by *GNLY*) is negative in $GZMB^+$ B cells and $GZMB^+$ PCs; $GZMB^+$ B cells were CD19-positive but granulysin-negative, and $GZMB^+$ PCs were BCR light chain-positive but granulysin-negative. Second, the expression of *GZMB* (encoding granzyme B) was markedly lower than *GNLY* expression in B_BCR^+GNLY^+ cells (Extended Data Fig. 1d). Thus, B_BCR^+GNLY^+ cells may represent a unique "cytotoxic" cluster of B cells in humans and are particularly enriched in a specific window during childhood. The exact functions of this unique cytotoxic B-cell subset are currently unclear. Our independent analyses showed that, among the five B-cell subsets, B_BCR^+GNLY^+ cells were closest to the terminally differentiated mature B-cell type plasma cells: 1) both the B_BCR^+GNLY^+ cell and plasma cell subsets exhibited a similar unimodal pattern over the lifespan, peaking in 6-year-olds; and 2) B_BCR^+GNLY^+ cells were closest to plasma cells in terms of the developmental trajectories, transcriptional profiles, immunoglobulin isotype distributions, and BCR clonotypes. These results suggest that B_BCR^+GNLY^+ cells are in a later stage, close to plasma cells, during the differentiation of B lymphocytes. However, B_BCR^+GNLY^+ cells exhibit distinct characteristics. Unlike plasma cells, B_BCR^+GNLY^+ cells highly express cytotoxic genes, such as *GNLY* and *NKG7*. Moreover, functional analyses of GNLY-overexpressing human and mouse B cells showed

that GNLY-overexpressing B cells exhibited cytotoxic behavior on bacterial proliferation. B-cell functions mature in individuals by approximately ten years old[38].

2.2. Two peaks of T-cell clonal expansions across the lifespan

Previous studies limited to adult population have shown elevated T-cell clonal expansion only at the elderly ages[39]. However, taking advantage of our lifecycle-wide cohort from birth to old age, we revealed that high T-cell clonal expansions actually exhibited two peaks at the extremes of the lifespan, with an early peak in the 2–12 y group and a late peak in the 70–90 y group. $CD8^+$ T cells are the main effectors in host defense against invading intracellular pathogens and existing malignant cells[40]. In the present study, CD8_TEM_GNLY cells exhibited the highest proportions of highly clonally expanded cells among all 11 αβ T-cell subsets. Further molecular feature analyses suggested that the functional significance underlying the clonal expansion of CD8_TEM_GNLY cells were significantly different in these two age categories. The high-TCE CD8_TEM_GNLY cells in children were characterized by high expression of cytotoxic genes, indicating that the cells are gaining increased killing function (e.g., against infected and cancerous cells) during development. In contrast, the high-TCE CD8_TEM_GNLY cells in elderly participants were characterized by the high expression of genes enriched in biological processes related to chronic inflammation. Considering the disparities in physiology and environmental exposure (i.e., infections and vaccination) between children and older people, our results may reflect distinct mechanisms between aging-related clonal expansion in the 70–90 y group (e.g., chronic inflammation-related) and development-related clonal expansion in the 2–12 y group (e.g., external stimulus-related). Notably, T-cell clonal expansion is accompanied by alteration of immune checkpoints[41, 42]. We observed differential expression features of immune checkpoints between the developing and elderly stages. The expression of immune checkpoints, including *CD27*, *ICOS*, and *PDCD1*, was enriched in children, while *IL15* was enriched in elderly participants. CD27[43] and ICOS[44] participate in T-cell activation and survival, while PD-1 (encoded by *PDCD1*) is a critical molecule involved the regulation of the in T-cell response, suppressing T-cell activity and amplification in the late stage of the immune response[45]. *IL-15*, as a homeostatic cytokine for T cells that controls inflammatory immune responses, can be targeted by antibodies or mutagenesis to alleviate inflammation-related diseases[46].

2.3. Limitations

The human immune systems begin to develop during the prenatal period, but our dataset did not include any fetal sample. Stras *et al*. created a comprehensive fetal intestinal immune landscape, including the establishment of immune system and BCR and TCR repertoires diversity as early as 16 weeks' gestational age using CyTOF and TCR/BCR repertoires sequencing[47]. This study complements our work in providing a holistic picture of immune system development in the fetal period. Although the present work provided a comprehensive single-cell resource of human peripheral immune cells spanning the entire lifespan, the age-related changes in certain rare cell subsets require exploration in further studies with larger sample size. Our cohort was composed of individuals of Asian descent, broad generalization of our results to world-wide populations should be approached with caution and requires further validation in ethnically different aging cohorts. There are many possible future directions based on this lifecycle-wide single-cell resource, more *in vitro* and *in vivo* functional experiments are a necessary next step for the age-associated genes and the potential aging biomarkers and cell–cell interactions identified in our study.

3. Supplementary Methods

3.1 Inclusion and exclusion criteria for participants

To avoid possible interference by other confounding factors, all participants met the strict healthy criteria originally developed for enrollment in the Baltimore Longitudinal Study of Aging[48] and in accordance with the WHO classification. Participants declared no specific disease issues. Participants with any of the following conditions were excluded: (1) cardio-cerebrovascular diseases (e.g., hypertension, coronary artery disease, congestive heart failure, and stroke); (2) neurodegenerative disorders or cognitive impairment; (3) endocrine and metabolic diseases (e.g., diabetes mellitus, dyslipidemia, and hypo- or hyperthyroidism); (4) hematological disorders; (5) renal or hepatic dysfunction; (6) infectious diseases (e.g., human immunodeficiency virus infection, human papillomavirus infection, hepatovirus infection, COVID-19 infection, and cytomegalovirus infection); (7) autoimmune diseases and motor dysfunctions; (8) cancer; (9) smoking; and (10) steroid usage and vaccination within three months.

3.2 Sample collection, preparation, and storage

Blood samples were collected from the peripheral vein of each donor and processed within 2 hours of collection. UCB was obtained from placental cords. PBMCs were separated using Vacutainer CPT tubes (362761, BD, San Diego, CA, USA) following the manufacturer's protocols[49]. The viability of the PBMCs in each sample was examined by Trypan Blue staining and confirmed to be >90%. PBMCs were immediately used for scRNA-seq library construction and sequencing, or they were cryopreserved at −80°C in a medium containing 10% dimethylsulfoxide and 90% fetal bovine serum for CyTOF experiments.

3.3 Identification of DEGs in peripheral immune cells

To investigate the effect of age on peripheral immune cells, we identified DEGs among the different life stages for each PBMC subset as follows: (1) for each cell subset in one sample, the synthetic bulk expression value for each gene was generated by dividing the gene-specific UMI count with the total number of UMIs in the cells and multiplying by 10,000 (CP10K); (2) ribosome and mitochondrial genes were removed in all samples; (3) genes with expression more than 1 (CP10K $\geq$ 1) in at least three samples were kept and analyzed by Kruskal-Wallis test; and 4) genes with a p value < 0.001 were considered to be DEGs. Age-related monotonical DEGs (M-DEGs)

were further determined using Spearman Rho analyses ($|\rho| \geq 0.6$, $P < 0.01$) based on all DEGs. CP10K was defined as:

$$CP10K_{i,k} = \frac{\sum_j e_{i,j,k}}{\sum_i \sum_j e_{i,j,k}} \cdot 10^4$$

where e is the number of UMIs of i gene defined by the unique molecular barcode of j cell in sample k. The M-DEGs shared by ≥ 5 cell subsets were defined as common M-DEGs.

To identify the DEGs in CD8_MAIT_SLC4A10 cells between the adolescent (12–18 y) group and other age groups, the Seurat built-in FindAllMarkers function (parameters: only.pos = F; min.pct = 0.25; logfc.threshold = 0.25; test = wilcox) was run comparing the adolescent group with other age groups. The FindAllMarkers function with the same parameter settings was also used to identify the DEGs in highly clonal expanded CD8_TEM_GNLY cells between the early-life (2–12 y) and late-life (70–90 y) high-TCE groups. The DEGs were filtered using a minimum $\log_2$(fold change) of 0.25 or a maximum $\log_2$(fold change) of -0.25 and an adjusted p value of 0.05. The DEG volcano plots were performed by the ggplot2 v3.5.1 package in R.

3.4 Functional enrichment analyses and gene set scoring

Functional enrichment analyses of DEGs were conducted using the R package clusterProfiler (v4.0.5)[50] using default parameters. GSEA of the marker genes of TCR^+ T-cell subsets was performed using the GSEA function in clusterProfiler based on the datasets 'c7:immunologic gene sets' collected from the Molecular Signatures Database (MSigDB)[51].

3.5 CCI analyses

Manually curated human ligand–receptor interaction pairs were downloaded from the CellTalkDB database[6]. For each sample, the interaction strength was calculated between cell subset i and cell subset j. The ligand and receptor in a pair (LR) are L and R, respectively. For cell subset i and cell subset j, their interaction strength was defined as:

$$S_{i,j} = \sum_{k=1}^{N} L_{k,i} * R_{k,j} + \sum_{k=1}^{N} R_{k,i} * L_{k,j}$$

where $L_{k,i}$ and $R_{k,i}$ represent the total UMI count of ligand L_k and receptor R_k expressed in cell subset i, $L_{k,j}$ and $R_{k,j}$ represent the total UMI count of ligand L_k and receptor R_k expressed in cell

subset *j,* and *N* is the total number of LR pairs. For each sample, the CCI strength between cell subset *i* and cell subset *j* was sum normalized and the normalized CCI strength ($P_{i,j}$) was defined as :

$$P_{i,j} = \frac{S_{i,j}}{\sum_{\substack{1 \le j \le (M-1) \\ i<j \le M}} S_{i,j}}$$

Kruskal-Wallis test was used to calculate the significance of the p values of $P_{i,j}$ among samples from different age groups to identify CCIs that varied significantly with age. Kruskal-Wallis test was also used to identify differentially-expressed ligands and receptors among different age groups ($P < 0.05$, CP10K ≥ 0.01 in at least three samples). Experimentally validated immune checkpoint targets in cancer immunotherapy were downloaded from the CKTTD database[52] and their expression dynamics were examined in different cell subsets across the human lifespan. The networks were visualized with Cytoscape (v3.10.1), and the tool NetworkAnalyzer was used to calculate the degree and betweenness of each node.

3.6 Comparison of transcriptomes of immune cell subsets

MetaNeighbor analyses[53] were performed through neighbor voting based on the Spearman correlation between pseudo-cells of different immune cell subsets to compare immune cell subset transcriptomes. A pseudo-cell was made by aggregating 10 cells randomly selected from the same cell type derived from the same group to reduce the effects of outliers and noise[54]. Mean receiver operating characteristic (ROC) curve scores were acquired from MetaNeighbor. The pheatmap package in R was adopted to visualize transcriptome similarity.

3.7 TF analyses

After arranging the gene cell matrix into appropriate input format, the SCENIC[19] package (v1.3.1) in R was used to evaluate the TFs of individual immune cell subset following the default parameters. The pheatmap and ggplot2 packages in R were used to visualize the expression profile of TFs.

3.8 Immunofluorescence staining

Fresh PBMCs were separated using vacutainer CPT tubes (362761, BD) and resuspended with 1×10^6 cells/ml in 1–2 ml of 1 × PBS. The cells were prepared on SuperFrost plus slides using a

Shandon Cytospin 4 (Thermo Fisher Scientific, Lafayette, CO, USA)[55]. After fixation in 4% paraformaldehyde, PBMCs were permeabilized with 0.1% Triton X-100 and blocked in PBS with 10% BSA at room temperature. Fixed PBMCs were incubated with primary antibodies against IgM (1:500, 14-9998-82, Thermo Fisher Scientific), IgA (1:500, SC-166634, Santa Cruz, CA, USA), J chain (1:500, MA5-25840, Thermo Fisher Scientific), and granulysin (1:500, ab241333, Abcam, MA, USA) overnight at 4°C, followed by incubation with an Alexa Fluor 488-conjugated secondary antibody (1:200, A-10680, Thermo Fisher Scientific) or Alexa Fluor 555-conjugated secondary antibody (1:200, A-31572, Thermo Fisher Scientific). Counterstaining was performed with 4'-6-diamidino-2-phenylindole. The stained PBMCs were viewed by fluorescence microscopy (TCS SP8, Leica)[56].

3.9 Flow cytometric analyses

Fresh PBMCs were separated using vacutainer CPT tubes (362761, BD) and suspended in FACS buffer (554656, BD). Human Fc block (1:20, 564220, BD) was used to prevent nonspecific binding. Fixable live/dead viability dye (1:1000, 564406, BD) was used to determine cell viability. Monoclonal antibodies specific for human IgM (1:200, 551062, BD), granulysin (1:100, 558254, BD), IgD (1:100, 348232, BD), and CD19 (1:200, 566396, BD) were purchased from BD Pharmingen. For intracellular staining, the Fixation/Permeabilization Solution Kit (554714, BD) was used following the manufacturer's protocols. Flow cytometry experiments were performed on a BD FACS LSRFortessa, and the data were processed and analyzed using FlowJo (v10.8.1, Tree Star, Ashland, OR, USA) software.

3.10 B-cell clonal expansion analysis

10× CellRanger VDJ output was realigned to the IMGT reference with Change-O software (v1.3.0)[57]. Cells with no productive heavy chain sequence, multiple heavy chain sequence, or no gene expression information were excluded for downstream analysis. Next, hierarchicalClones function in the SCOPer R package (v1.3.0)[58] was used to identify B-cell clonotypes. B-cell clonal expansion score for each subtype was calculated using the STARTRAC R package (v0.1.0)[18].

3.11 T-cell STARTRAC analysis

T-cell clonotypes were identified using the CDR3 nucleotide sequence of both TCR α-chain and β-chain. T-cell clonal expansion score for each subtype was calculated using the STARTRAC R

package (v0.1.0)[18]. STARTRAC-expa is used to measure the degree of clonal expansion T-cell subsets upon TCR tracking.

3.12 B-cell trajectories and pseudotime analyses

Monocle2 (v2.6.1)[17] was used to estimate the pseudo temporal path of B-cell differentiation. The differentialGeneTest function in Monocle2 was adopted to identify the "ordering_genes" using the default parameters. The DDRTree algorithm was used for dimensionality reduction.

3.13 Plasmid construction and cell transfection

Human GNLY cDNA was cloned into the pcDNA3.0 expression vector[127]. Briefly, cDNA from human PBMCs was used as the template for amplifying the coding region of *GNLY*. The amplified sequence containing the coding region of *GNLY*, Kozak sequences and restriction sites (HindIII and EcoRI), was then inserted into the pcDNA3.0 expression vector. All restriction enzymes were obtained from TAKARA (Japan). All constructs were verified by DNA sequencing. For the generation of *GNLY*$^+$ human B cells, freshly isolated human B cells were transfected with *GNLY* overexpression plasmid by electroporation using the Nucleofector Kit (V4XP-3024, Lonza, Walkersville, MD, USA)[59]. pcDNA3.0 empty vector was used as a negative control. After 48 h, transfected B cells were subjected to flow cytometry for determination of the overexpression efficiency.

3.14 Generation of transgenic mice overexpressing human *GNLY*

The protocols for randomized animal experiments were approved by the Institute's Animal Ethics Committee of Shanghai Jiao Tong University, School of Medicine, Renji Hospital and adhered to the NIH Guidelines for the Care and Use of Laboratory Animals. To generate mice with overexpression of *GNLY*, cDNA for human *GNLY* was cloned and used to construct the transgene vector CAG-loxP-STOP-loxP-GNLY-WPRE-pA (Shanghai Model Organisms Center, Inc). The transgene vector was knocked in at the ROSA26 locus using CRISPR/Cas9 methods. To induce B-cell specific *GNLY* expression, CAG-loxP-STOP-loxP-GNLY-WPRE-pA TG mice were bred with CD19-CAG-Cre transgenic mice; littermate CD19-Cre mice were used as controls. Both male and female mice used in this study were on a C57BL/6 background and between 6-8 weeks of age. All mice were kept at 24°C ± 2°C, humidity of 40% ± 5%, under a constant 12-hour light/dark cycle with free access to diet and water. Tail genomic DNA was amplified by PCR using the GNLY

gene-specific probes GNLY 5' exon 1 (5'-GGGCCCTCCTGCTCCTTGCAGCCATGCTCCTGGGC-3') and 3' exon 2 (5'-GCAGGGTGCAGGGGGCAGGAAGTCTGCCTTGAACA-3'), generating a 195-bp product. For CD19-Cre, the 200 bp and 280 bp bands represent CD19-Cre^{+} and CD19-Cre^{-}, respectively.

3.15 Mouse B cell isolation and purification

Mouse B cells were isolated and purified from single-cell suspensions of mouse spleens by magnetic negative selection using a Mouse Pan B Cell Isolation Kit (130-095-813, Miltenyi Biotec). The purity of the isolated B cells was determined by flow cytometry. B cells with purity over 95% were cultured in six-well plates (5×10^5 cells per well) in RPMI-1640 media (Gibco) containing 10% FBS, 100 U/mL penicillin, and 100 ng/mL streptomycin.

3.16 Determination of B-cell bactericidal activity

Human GNLY-overexpressing B cells (5×10^5/200 μL of medium without antibiotic) and controls (control-transfected B cells and non-transfected B cells), and mouse B cells isolated from transgenic mice with human *GNLY* overexpression and littermate CD19-Cre mice were used. Cells were cultured with 5×10^3 CFU of *S. aureus* or *S. pneumoniae* for 6 h in 5% CO_2 at 37°C[60]. The culture medium was serially diluted 10-fold with phosphate buffered saline and plated using a spiral plater on agar plates; the plates were incubated at 37°C for 24 h. The number of colonies on the agar plates was counted.

3.17 GNLY^{+} B cell expansion and characterization

Cytotoxic immune cells (e.g., cytotoxic T cells/NK cells) can be induced by *in vitro* stimulation[61, 62]. Previous studies have reported that cytotoxic B cells can also be induced in human primary B cells by different protocols[34, 35, 37, 63]. In our pilot study, GNLY-expressing B cells were more efficiently induced using an expansion mixture containing interleukin (IL)-21, IL-2, CD40 ligand (CD40L), F(ab')$_2$ anti-BCR Abs, and CpG ODN 2006[63] compared with other expansion mixtures. Thus, we used this expansion mixture in all experiments.

Sorted B cells (1.5×10^6 cells/ml) were cultured for 1 or 3 days with combinations of IL-21 (10 ng/ml, 10584-HNAE, Sinobiological, Beijing, China), F(ab')$_2$ anti-BCR Abs (5 mg/ml, 109-006-064, Jackson Immunoresearch, West Grove, PA, USA), CpG ODN 2006 (1 mg/ml, tlrl-2006, InvivoGen, San Diego, CA, USA), CD40L (50 ng/ml, 10239-H01H, Sinobiological), and IL-2 (50

IU/ml, GMP-11848-HNAE, Sinobiological). Cells were treated with brefeldin A (1 μg/ml, HY-16592, MCE, Beijing, China) 4 h before immunofluorescent staining for flow cytometric analyses to detect intracellular granulysin. Cells were stained with Fixable live/dead viability dye (564406, BD) to identify dead cells, followed by staining for CD19 (566396, BD), IgM (551062, BD), and granulysin (558254, BD). After exclusion of dead cells and doublets, B lymphocytes were identified on a BD FACS LSRFortessa based on their morphological features and indicated target molecule expression. Data were analyzed using FlowJo (v10.8.1., Tree Star, Ashland, OR, USA) software.

3.18 Human MAIT-cell isolation and expansion

Human peripheral MAIT cells were isolated and purified by immunomagnetic separation, following the manufacturer's manual. A biotinylated anti-Vα7.2 (130-100-187, Miltenyi) antibody and the anti-Biotin MicroBeads (130-090-485, Miltenyi) were adopted for MAIT cell isolation[64]. Once completed, the MAIT cells were expanded in serum-free and xeno-free ImmunoCult-XF T cell expansion medium (10981, STEMCELL Technologies) for six days[65].

3.19 Determination of MAIT-cell antimicrobial activity

The antimicrobial activity of the MAIT cells was determined by intracellular bacteria enumeration in target cells that had been infected by *E. coli* and co-cultured with MAIT cells. Briefly, *E. coli* strains were cultured on tryptic soy agar supplemented with 4% defibrinated sheep blood. The next day, they were suspended in PBS, enumerated by optical spectrometry, and diluted to 1×10^8 CFU/mL (we verified the CFU counts by plating on appropriate agar overnight). Then, we picked the HeLa cell lines for live *E.* coli infection at 37°C/5% CO_2 for 3 h. They were used as target cells for subsequent bacterial enumeration after co-culturing with MAIT cells. After infection, target cells were processed as follows: 1) washed by PBS 4-6 times; 2) cultured at 37°C/5% CO_2 for another 1 h in complete RPMI-1640 medium supplemented with 200 μg/mL gentamicin (Gibco) to eliminate extracellular bacteria; and 3) washed sufficiently by serum-free and antibiotics-free RPMI-1640 medium. Subsequently, target cells were co-cultured with MAIT cells at an E:T ratio of 5:1 and incubated for 3 h at 37°C/5% CO_2. Last, we visually inspected the live bacteria enumeration after lysing adherent cells with 0.1% Triton-X for 10 min at room temperature and plating collected lysates onto LB agar plates at 37°C for 24 h.

3.20 Human umbilical vascular endothelial cells (HUVECs) isolation, culture and *in vitro* aging model construction

HUVECs were isolated and pooled from umbilical cords obtained from normal vaginal deliveries [66]. In brief, HUVECs were isolated using 0.1% type 1 collagenase (LS004196, Worthington) and cultured with Endothelial Cell Medium (#1001, ScienCell) with fatal bovine serum (No.0025, ScienCell), endothelial cell growth supplement (No.1052, ScienCell), and antibiotic solution (No.0503, ScienCell). To construct *in vitro* HUVECs aging model, HUVECs were serially cultured to different passages including passage 3 (P3), passage 5 (P5), passage 7 (P7), and passage 9 (P9) in a time-course experiment.

3.21 RNA isolation and reverse transcription quantitative polymerase chain reaction (RT-qPCR)

Total RNA was extracted using TRIzol reagent (T9108, TAKARA). The NanoDrop spectrophotometer was employed to assess the concentration and purity of the isolated RNA. Next, the isolated RNA was reverse transcribed into complementary DNA (cDNA) using HiScript® III RT SuperMix for qPCR (+gDNA wiper) (R212, Vazyme). qPCR analysis was conducted using ChamQ SYBR qPCR Master Mix (Q711-02, Vazyme) in LightCycler 480II (Roche). Melting curve analysis was employed to ascertain primer specificity. The normalization of target gene expression levels was performed relative to *GAPDH*, and details of the primer information are shown in Supplementary Table 11.

3.22 SA-β-galactosidase activity assay

SA-β-galactosidase activity was examined to evaluate the senescence of the HUEVCs. Briefly, cells were washed with PBS and then fixed with fixation buffer supplied by the manufacturer (C0602, BeyoGold™) for 10 minutes at room temperature. The fixed cells were washed twice with PBS before addition of 1 mg/ml X-gal in N,N-dimethylformamide, 2 mM $MgCl_2$, 150 mM NaCl, 5 mM potassium ferricyanide, 5 mM potassium ferrocyanide, 40 mM citric acid/Na phosphate buffer, pH 6.0. Cells were incubated with the staining solution overnight at 37 °C and washed twice with H_2O and examined using an inverted light microscope (CKX3-SLP, OLYMPUS).

4. Supplementary Figures

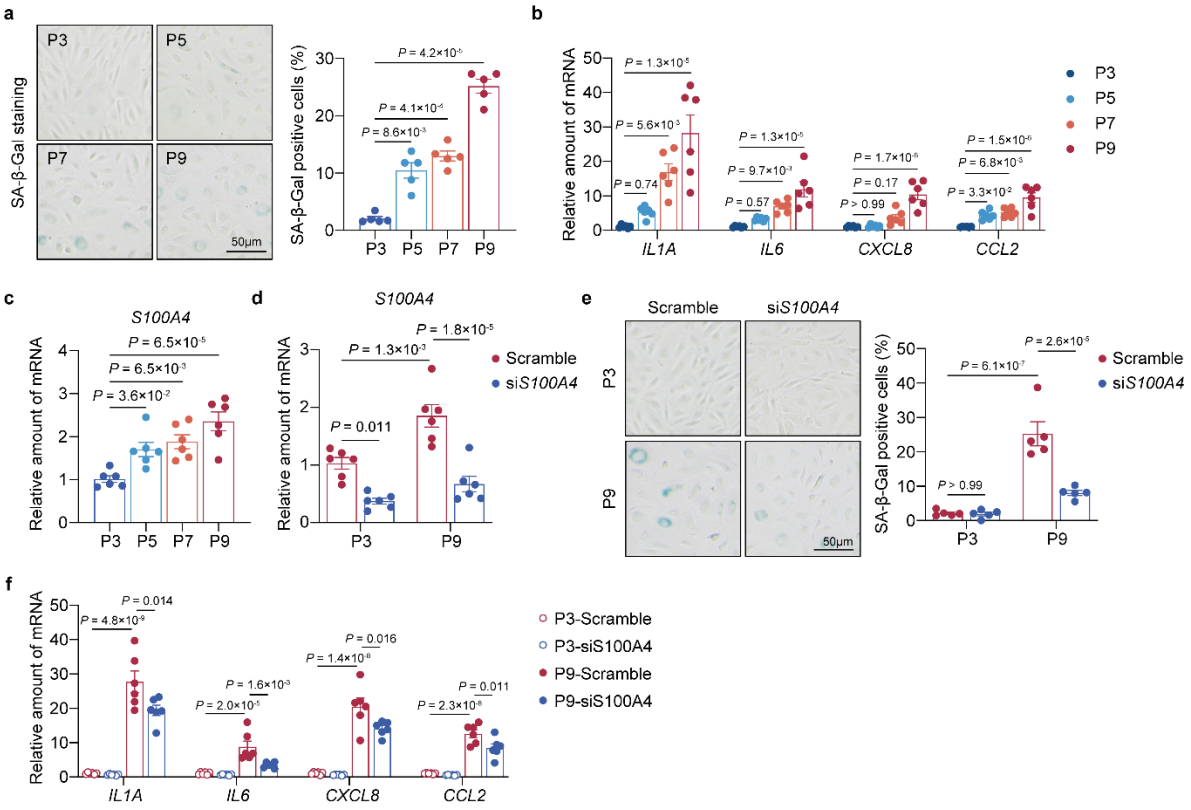

Supplementary Fig. 1 | Exploring the function of *S100A4* in an *in vitro* aging model.

a. Representative images (left) and quantification (right) of SA-β-Gal staining of HUVECs at passage 3, 5, 7 and 9 (P3, P5, P7, and P9) (n = 5 per group).

b. mRNA expressions of *IL1A*, *IL6*, *CXCL8*, and *CCL2* were measured by RT-qPCR in HUVECs at P3, P5, P7, and P9 (n = 6 per group).

c. *S100A4* mRNA expression was measured by RT-qPCR in HUVECs at P3, P5, P7, and P9 (n = 6 per group).

d. HUVECs at P3 and P9 were transfected with scramble siRNA (Scramble) or *S100A4* siRNA (siS100A4) for 48 h. After treatment, *S100A4* mRNA expression was measured by RT-qPCR in HUVECs (n = 5 per group). .

e. HUVECs at P3 and P9 were transfected with scramble siRNA (Scramble) or *S100A4* siRNA (siS100A4) for 48 h. Post-treatment representative images (left) and quantification (right) of SA-β-Gal staining of HUVECs were shown (n=6 per group).

f. HUVECs at P3 and P9 were transfected with scramble siRNA (Scramble) or *S100A4* siRNA (siS100A4) for 48 h. After treatment, mRNA expressions of *IL1A*, *IL6*, *CXCL8*, and *CCL2* were measured by RT-qPCR in HUVECs (n=6 per group).

Error bars represent mean ± SEM. A p value < 0.05 was considered statistically significant. P values were determined by one-way ANOVA followed by the Tukey post-hoc test in (**a**)–(**c**). P values were determined by two-way ANOVA followed by the Tukey post-hoc test in (**d**)–(**f**).

ANOVA, analysis of variance; HUVECs, human umbilical vein endothelial cells.

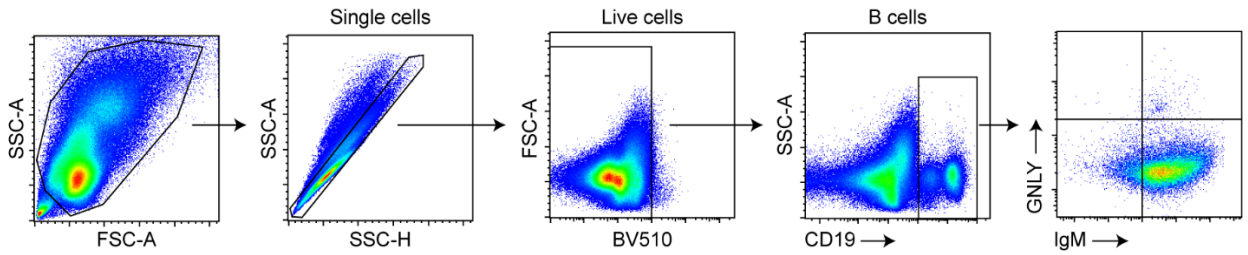

Supplementary Fig. 2 | Gating strategy for newly discovered cytotoxic B-cell subset (B_BCR^{+}GNLY^{+} cells). Flow cytometry analysis using antibodies specific for CD19, IgM, and GNLY to characterize the cytotoxic B-cell subset.

IgM, Immunoglobulin M; GNLY, Granulysin.

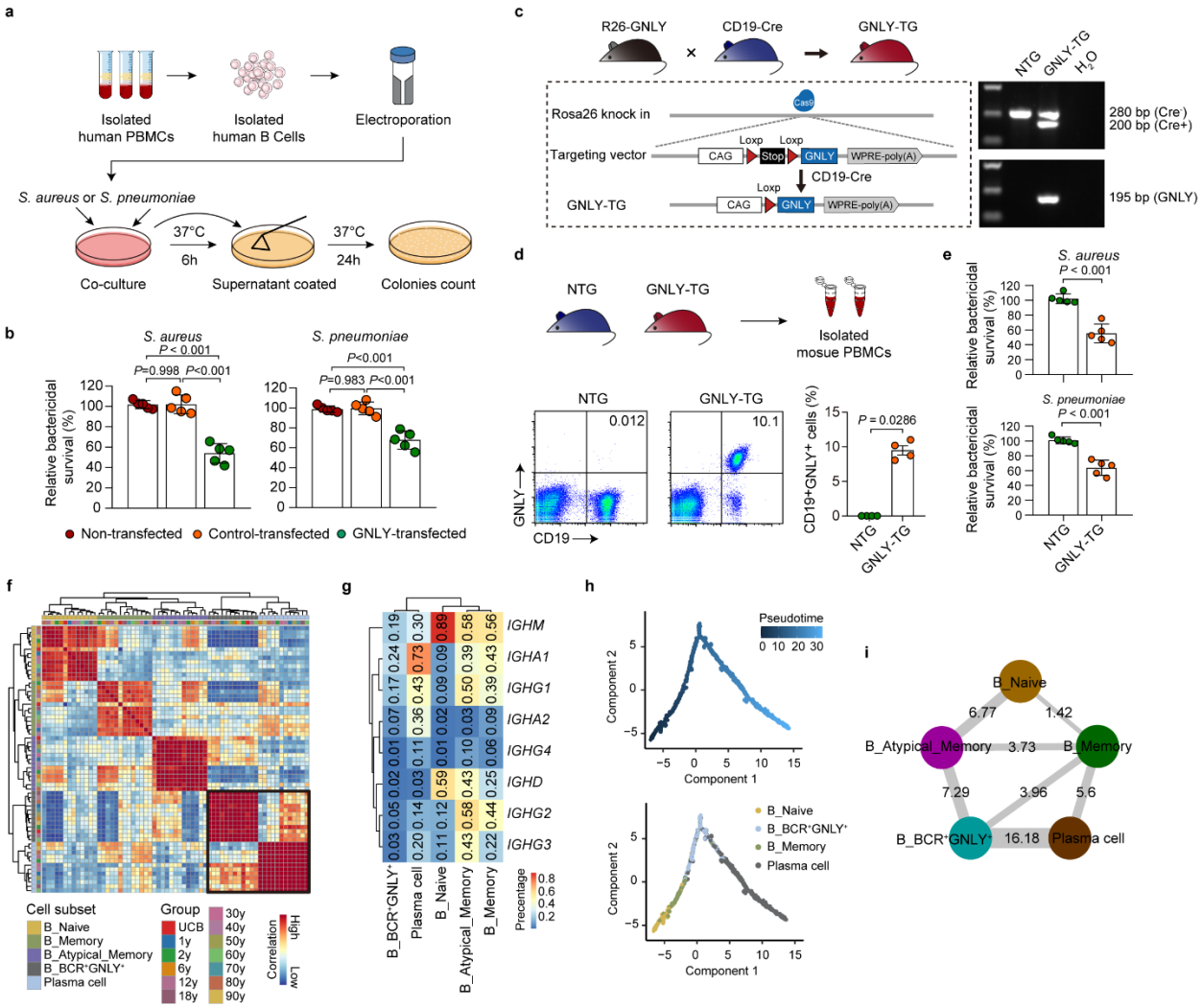

Supplementary Fig. 3 | Function of the newly identified cytotoxic B-cell subset (B_BCR$^+$GNLY$^+$ cells).

a. Schematic diagram detailing the assay on bactericidal effects against *S. aureus* or *S. pneumoniae* for isolated B cells that overexpressing GNLY by electroporation.

b. Bar plots showing the bactericidal effects of GNLY-overexpressing B cells against *S. aureus* (left panel) or *S. pneumoniae* (right panel) (n = 5 per group). P values were determined by one-way ANOVA followed by the Tukey post-hoc test.

c. Schematic diagram of gene editing strategy for transgenic mice overexpressing human GNLY (top panel). To generate B-cell-specific GNLY-overexpression (GNLY-TG) mice, R26-GNLY (NTG) mice were crossed with the mice carrying the CD19-Cre transgene. PCR analysis was performed for the confirmation of successful gene editing (bottom panel). The 195 bp band

represents the GNLY gene, which was produced by the insertion of GNLY cDNA at Rosa26 locus. The 200 bp and 280 bp bands represent CD19-Cre^{+} and CD19-Cre^{-}, respectively. This experiment was independently repeated three times with similar results.

d. Flow cytometry scatter plots showing proportions of CD19^{+}GNLY^{+} cells in PBMCs isolated from GNLY-TG and NTG mice (left and middle panels). Bar plots showing the percentage of CD19^{+}GNLY^{+} cells in GNLY-TG and NTG mice (right panel) (n = 4 per group). P values were determined by the two-sided unpaired Wilcoxon runk-sum test.

e. The bactericidal effects of B cells derived from GNLY-TG and NTG mice against *S. aureus* or *S. pneumoniae* (n = 5 per group). P values were determined by the two-sided unpaired *t* test.

f. Heatmap showing the correlation of gene expression among different B-cell subsets.

g. Heatmap showing the UMI percentage of immunoglobulin heavy-chain genes (*IGHA1*, *IGHA2*, *IGHD*, *IGHG1*, *IGHG2, IGHG3*, *IGHG4,* and *IGHM*) in each B-cell subset. Numbers represent the actual percentage values.

h. The order of B-cell subsets along pseudotime determined by Monocle2. Each dot represents a single cell.

i. Network plot showing the ratio of shared BCR clones between any two cell subsets. The width of the lines is proportional to the ratio.

Error bars represent mean ± SEM. A p value < 0.05 was considered statistically significant.

BCR, B-cell receptor; PBMCs, peripheral blood mononuclear cells; UMI, unique molecular identifier.

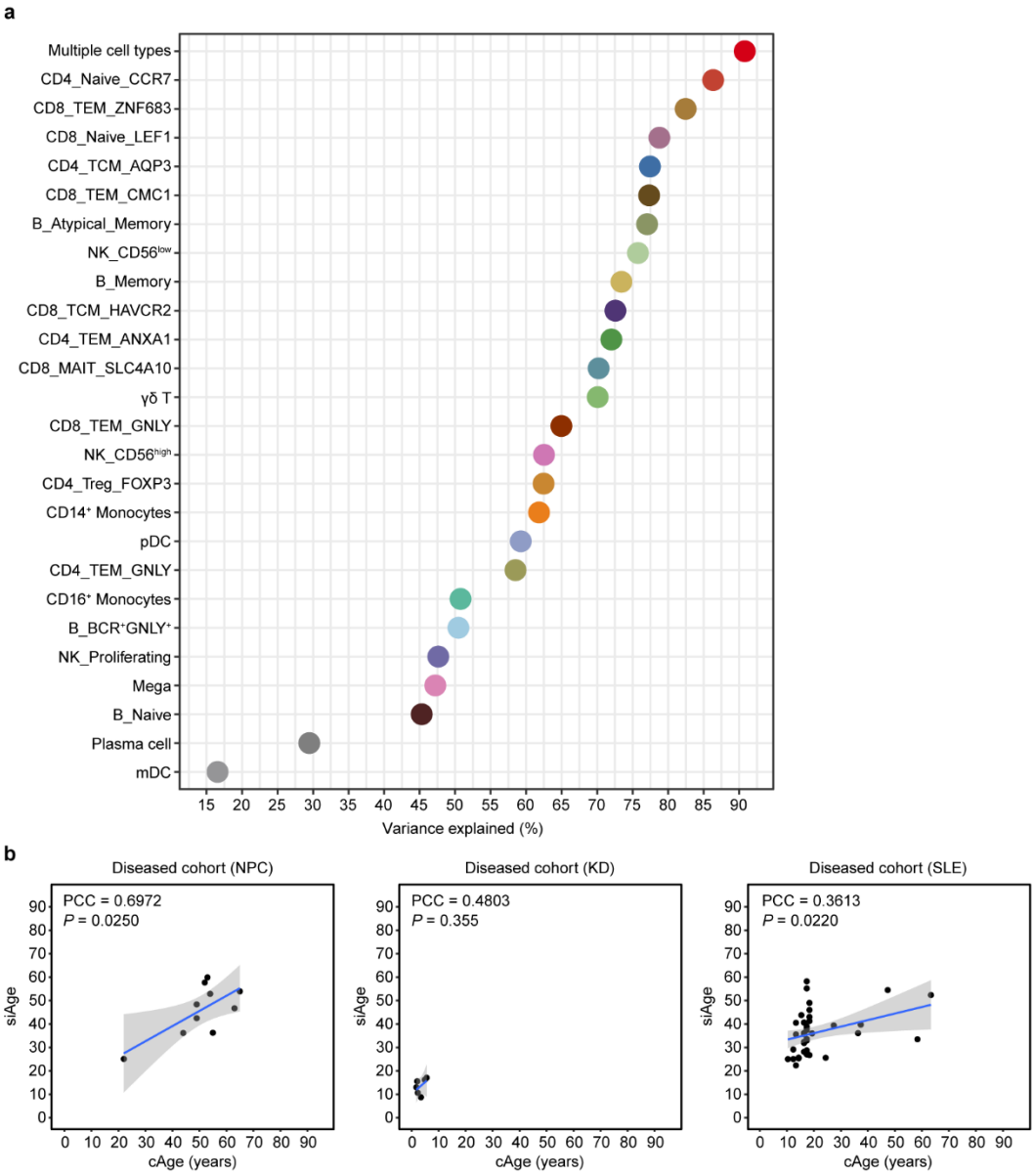

Supplementary Fig. 4 | Assessment of the single-cell immune age predictive model.

a. Dot plot showing the predictive performance of the cell type-specific immune age prediction model based on our lifecycle-wide single-cell data. All cell types are shown.

b. Scatter plots showing the correlation of single-cell immune age (siAge) with chronological age (cAge) in the validation cohorts of patients with disturbed immune function: NPC (n = 10 samples), SLE (n = 40 samples), and KD (n = 6 samples) cohort. The blue line indicates linear regression. The gray shadow covers the 95% confidence interval. PCC and p values are indicated. A p value < 0.05 was considered statistically significant.

KD, Kawasaki diseases; NPC, nasopharyngeal carcinoma; PCC, Pearson correlation coefficient; SLE, systemic lupus erythematosus.

5. Supplementary Table List

Supplementary Table 1. Characteristics of healthy participants across the entire human lifespan.

Supplementary Table 2. Characteristics of the healthy and diseased validation cohorts for siAge prediction model.

Supplementary Table 3. Marker genes of 25 distinct PBMC subsets defined by scRNA-seq.

Supplementary Table 4. Antibody panels used for high-throughput CyTOF analyses in this study.

Supplementary Table 5. Monotonical differentially-expressed genes associated with age in 25 cell subsets.

Supplementary Table 6. Functional enrichment analyses of monotonical differentially-expressed genes associated with age.

Supplementary Table 7. Age-related genes in bulk RNA-seq data.

Supplementary Table 8. Differentially-expressed ligands and receptors across the entire lifespan.

Supplementary Table 9. Dynamics of differentially-expressed immune checkpoint expression in 25 cell subsets across the entire lifespan.

Supplementary Table 10. Signature genes of each B-cell subset.

Supplementary Table 11. The information of PCR primers.

6. Supplementary References

1. Bloom, S.I., Islam, M.T., Lesniewski, L.A. & Donato, A.J. Mechanisms and consequences of endothelial cell senescence. *Nat Rev Cardiol* **20**, 38-51 (2023).
2. Hao, S. *et al.* Network Approaches for Dissecting the Immune System. *iScience* **23**, 101354 (2020).
3. Rieckmann, J.C. *et al.* Social network architecture of human immune cells unveiled by quantitative proteomics. *Nat Immunol* **18**, 583-593 (2017).
4. Jin, S. *et al.* Inference and analysis of cell-cell communication using CellChat. *Nat Commun* **12**, 1088 (2021).
5. Efremova, M., Vento-Tormo, M., Teichmann, S.A. & Vento-Tormo, R. CellPhoneDB: inferring cell-cell communication from combined expression of multi-subunit ligand-receptor complexes. *Nat Protoc* **15**, 1484-1506 (2020).
6. Shao, X. *et al.* CellTalkDB: a manually curated database of ligand-receptor interactions in humans and mice. *Brief Bioinform* **22** (2021).
7. Poli, A. *et al.* CD56bright natural killer (NK) cells: an important NK cell subset. *Immunology* **126**, 458-465 (2009).
8. Oja, A.E. *et al.* The Transcription Factor Hobit Identifies Human Cytotoxic CD4(+) T Cells. *Front Immunol* **8**, 325 (2017).
9. Yang, Y.H. *et al.* Deficiency of annexin A1 in CD4+ T cells exacerbates T cell-dependent inflammation. *J Immunol* **190**, 997-1007 (2013).
10. Hasegawa, T. *et al.* Cytotoxic CD4(+) T cells eliminate senescent cells by targeting cytomegalovirus antigen. *Cell* **186**, 1417-1431 e1420 (2023).
11. Shannon, P. *et al.* Cytoscape: a software environment for integrated models of biomolecular interaction networks. *Genome Res* **13**, 2498-2504 (2003).
12. Wang, P. *et al.* Identification of lncRNA-associated competing triplets reveals global patterns and prognostic markers for cancer. *Nucleic Acids Res* **43**, 3478-3489 (2015).
13. Przulj, N., Wigle, D.A. & Jurisica, I. Functional topology in a network of protein interactions. *Bioinformatics* **20**, 340-348 (2004).
14. Buchan, S.L., Rogel, A. & Al-Shamkhani, A. The immunobiology of CD27 and OX40 and their potential as targets for cancer immunotherapy. *Blood* **131**, 39-48 (2018).
15. Dotiwala, F. & Lieberman, J. Granulysin: killer lymphocyte safeguard against microbes. *Curr Opin Immunol* **60**, 19-29 (2019).
16. Oracki, S.A., Walker, J.A., Hibbs, M.L., Corcoran, L.M. & Tarlinton, D.M. Plasma cell development and survival. *Immunol Rev* **237**, 140-159 (2010).
17. Qiu, X. *et al.* Reversed graph embedding resolves complex single-cell trajectories. *Nat Methods* **14**, 979-982 (2017).
18. Zhang, L. *et al.* Lineage tracking reveals dynamic relationships of T cells in colorectal cancer. *Nature* **564**, 268-272 (2018).

19. Aibar, S. *et al.* SCENIC: single-cell regulatory network inference and clustering. *Nat Methods* **14**, 1083-1086 (2017).

20. Pal, R. *et al.* C/EBPbeta regulates transcription factors critical for proliferation and survival of multiple myeloma cells. *Blood* **114**, 3890-3898 (2009).

21. Iwakoshi, N.N., Lee, A.H. & Glimcher, L.H. The X-box binding protein-1 transcription factor is required for plasma cell differentiation and the unfolded protein response. *Immunol Rev* **194**, 29-38 (2003).

22. Outram, S.V. *et al.* KLF13 influences multiple stages of both B and T cell development. *Cell Cycle* **7**, 2047-2055 (2008).

23. Sampieri, L., Di Giusto, P. & Alvarez, C. CREB3 Transcription Factors: ER-Golgi Stress Transducers as Hubs for Cellular Homeostasis. *Front Cell Dev Biol* **7**, 123 (2019).

24. Fritz, F., Preissner, R. & Banerjee, P. VirtualTaste: a web server for the prediction of organoleptic properties of chemical compounds. *Nucleic Acids Res* **49**, W679-W684 (2021).

25. Schattgen, S.A. *et al.* Integrating T cell receptor sequences and transcriptional profiles by clonotype neighbor graph analysis (CoNGA). *Nat Biotechnol* **40**, 54-63 (2022).

26. Karanika, S. *et al.* GLIPR1-DeltaTM synergizes with docetaxel in cell death and suppresses resistance to docetaxel in prostate cancer cells. *Mol Cancer* **14**, 122 (2015).

27. Ballar, P. *et al.* Identification of SVIP as an endogenous inhibitor of endoplasmic reticulum-associated degradation. *J Biol Chem* **282**, 33908-33914 (2007).

28. Pfistershammer, K. *et al.* CD63 as an activation-linked T cell costimulatory element. *J Immunol* **173**, 6000-6008 (2004).

29. Feng, Z. *et al.* Reduced expression of proteolipid protein 2 increases ER stress-induced apoptosis and autophagy in glioblastoma. *J Cell Mol Med* **24**, 2847-2856 (2020).

30. Novershtern, N. *et al.* Densely interconnected transcriptional circuits control cell states in human hematopoiesis. *Cell* **144**, 296-309 (2011).

31. Ny, L. *et al.* The plasminogen receptor, Plg-R(KT), plays a role in inflammation and fibrinolysis during cutaneous wound healing in mice. *Cell Death Dis* **11**, 1054 (2020).

32. Parcelier, A. *et al.* AF1q/MLLT11 regulates the emergence of human prothymocytes through cooperative interaction with the Notch signaling pathway. *Blood* **118**, 1784-1796 (2011).

33. Aman, Y. *et al.* Autophagy in healthy aging and disease. *Nat Aging* **1**, 634-650 (2021).

34. Hagn, M. *et al.* CD5+ B cells from individuals with systemic lupus erythematosus express granzyme B. *European journal of immunology* **40**, 2060-2069 (2010).

35. Boldrini, V.O. *et al.* Cytotoxic B Cells in Relapsing-Remitting Multiple Sclerosis Patients. *Front Immunol* **13**, 750660 (2022).

36. Arabpour, M., Rasolmali, R., Talei, A., Mehdipour, F. & Ghaderi, A. Granzyme B production by activated B cells derived from breast cancer-draining lymph nodes. *Molecular immunology* **114**, 172-178 (2019).

37. Xu, W. *et al.* Human plasma cells express granzyme B. *Eur J Immunol* **44**, 275-284 (2014).

38. Ghraichy, M. *et al.* Maturation of the Human Immunoglobulin Heavy Chain Repertoire With Age. *Front Immunol* **11**, 1734 (2020).

39. Sun, X. *et al.* Longitudinal analysis reveals age-related changes in the T cell receptor repertoire of human T cell subsets. *J Clin Invest* **132** (2022).

40. Belz, G.T. & Kallies, A. Effector and memory CD8+ T cell differentiation: toward a molecular understanding of fate determination. *Curr Opin Immunol* **22**, 279-285 (2010).

41. Pardoll, D.M. The blockade of immune checkpoints in cancer immunotherapy. *Nat Rev Cancer* **12**, 252-264 (2012).

42. Krekorian, M. *et al.* Imaging of T-cells and their responses during anti-cancer immunotherapy. *Theranostics* **9**, 7924-7947 (2019).

43. van Gisbergen, K.P. *et al.* The costimulatory molecule CD27 maintains clonally diverse CD8(+) T cell responses of low antigen affinity to protect against viral variants. *Immunity* **35**, 97-108 (2011).

44. Dong, C. *et al.* ICOS co-stimulatory receptor is essential for T-cell activation and function. *Nature* **409**, 97-101 (2001).

45. Wei, S.C. *et al.* Distinct Cellular Mechanisms Underlie Anti-CTLA-4 and Anti-PD-1 Checkpoint Blockade. *Cell* **170**, 1120-1133.e1117 (2017).

46. Pilipow, K. *et al.* IL15 and T-cell Stemness in T-cell-Based Cancer Immunotherapy. *Cancer Res* **75**, 5187-5193 (2015).

47. Stras, S.F. *et al.* Maturation of the Human Intestinal Immune System Occurs Early in Fetal Development. *Dev Cell* **51**, 357-373 e355 (2019).

48. Shock, N. *et al.* Normal Human Aging: The Baltimore Study of Aging (Washington, DC: US Government Printing Office): NIH Publication; 1984.

49. Corkum, C.P. *et al.* Immune cell subsets and their gene expression profiles from human PBMC isolated by Vacutainer Cell Preparation Tube (CPT) and standard density gradient. *BMC Immunol* **16**, 48 (2015).

50. Yu, G., Wang, L.G., Han, Y. & He, Q.Y. clusterProfiler: an R package for comparing biological themes among gene clusters. *OMICS* **16**, 284-287 (2012).

51. Liberzon, A. *et al.* Molecular signatures database (MSigDB) 3.0. *Bioinformatics* **27**, 1739-1740 (2011).

52. Zhang, Y. *et al.* Checkpoint therapeutic target database (CKTTD): the first comprehensive database for checkpoint targets and their modulators in cancer immunotherapy. *J Immunother Cancer* **8** (2020).

53. Crow, M., Paul, A., Ballouz, S., Huang, Z.J. & Gillis, J. Characterizing the replicability of cell types defined by single cell RNA-sequencing data using MetaNeighbor. *Nat Commun* **9**, 884 (2018).

54. Han, X. *et al.* Construction of a human cell landscape at single-cell level. *Nature* **581**, 303-309 (2020).

55. Bender, C., Rodriguez-Calvo, T., Amirian, N., Coppieters, K.T. & von Herrath, M.G. The

healthy exocrine pancreas contains preproinsulin-specific CD8 T cells that attack islets in type 1 diabetes. *Sci Adv* **6** (2020).

56. Xu, L. *et al.* Melatonin differentially regulates pathological and physiological cardiac hypertrophy: Crucial role of circadian nuclear receptor RORalpha signaling. *J Pineal Res* **67**, e12579 (2019).

57. Gupta, N.T. *et al.* Change-O: a toolkit for analyzing large-scale B cell immunoglobulin repertoire sequencing data. *Bioinformatics* **31**, 3356-3358 (2015).

58. Nouri, N. & Kleinstein, S.H. Somatic hypermutation analysis for improved identification of B cell clonal families from next-generation sequencing data. *PLoS Comput Biol* **16**, e1007977 (2020).

59. Sohn, H.W., Krueger, P.D., Davis, R.S. & Pierce, S.K. FcRL4 acts as an adaptive to innate molecular switch dampening BCR signaling and enhancing TLR signaling. *Blood* **118**, 6332-6341 (2011).

60. Hasegawa, M. *et al.* Interleukin-22 regulates the complement system to promote resistance against pathobionts after pathogen-induced intestinal damage. *Immunity* **41**, 620-632 (2014).

61. Takeuchi, A. *et al.* CRTAM determines the CD4+ cytotoxic T lymphocyte lineage. *J Exp Med* **213**, 123-138 (2016).

62. Lucas, M., Schachterle, W., Oberle, K., Aichele, P. & Diefenbach, A. Dendritic cells prime natural killer cells by trans-presenting interleukin 15. *Immunity* **26**, 503-517 (2007).

63. Chesneau, M. *et al.* Efficient Expansion of Human Granzyme B-Expressing B Cells with Potent Regulatory Properties. *J Immunol* **205**, 2391-2401 (2020).

64. Le Bourhis, L. *et al.* MAIT cells detect and efficiently lyse bacterially-infected epithelial cells. *PLoS Pathog* **9**, e1003681 (2013).

65. Boulouis, C. *et al.* Human MAIT cell cytolytic effector proteins synergize to overcome carbapenem resistance in Escherichia coli. *PLoS Biol* **18**, e3000644 (2020).

66. Jaffe, E.A., Nachman, R.L., Becker, C.G. & Minick, C.R. Culture of human endothelial cells derived from umbilical veins. Identification by morphologic and immunologic criteria. *J Clin Invest* **52**, 2745-2756 (1973).